Title

MicroPET II: design, development and initial performance of an improved microPET scanner for small-animal imaging

Journal

Physics in Medicine and Biology, 48(11)

ISSN

0031-9155

Authors

Tai, Y C
Chatziioannou, A F
Yang, Y F
et al.

Publication Date

2003-06-01

Peer reviewed

INSTITUTE OF PHYSICS PUBLISHING PHYSICS IN MEDICINE AND BIOLOGY

Phys. Med. Biol. **49** (2004) 2527–2545 PII: S0031-9155(04)75390-7

Optimization and performance evaluation of the microPET II scanner for *in vivo* small-animal imaging

Yongfeng Yang[1], Yuan-Chuan Tai[2], Stefan Siegel[3], Danny F Newport[3], Bing Bai[4], Quanzheng Li[4], Richard M Leahy[4] and Simon R Cherry[1]

[1] Department of Biomedical Engineering, University of California-Davis, One Shields Avenue, Davis, CA 95616, USA
[2] Department of Radiology, Washington University in St Louis, 510 S Kingshighway Boulevard, Box 8225, St Louis, MO 63110, USA
[3] Concorde Microsystems Inc., 10427 Cogdill Road Suite 500, Knoxville, TN 37932, USA
[4] Signal and Image Processing Institute, University of Southern California, 3740 McClintock Avenue, Los Angeles, CA 90089, USA

Received 29 January 2004
Published 26 May 2004
Online at stacks.iop.org/PMB/49/2527
DOI: 10.1088/0031-9155/49/12/005

Abstract

MicroPET II is a newly developed PET (positron emission tomography) scanner designed for high-resolution imaging of small animals. It consists of 17 640 LSO crystals each measuring 0.975 × 0.975 × 12.5 mm^3, which are arranged in 42 contiguous rings, with 420 crystals per ring. The scanner has an axial field of view (FOV) of 4.9 cm and a transaxial FOV of 8.5 cm. The purpose of this study was to carefully evaluate the performance of the system and to optimize settings for *in vivo* mouse and rat imaging studies. The volumetric image resolution was found to depend strongly on the reconstruction algorithm employed and averaged 1.1 mm (1.4 μl) across the central 3 cm of the transaxial FOV when using a statistical reconstruction algorithm with accurate system modelling. The sensitivity, scatter fraction and noise-equivalent count (NEC) rate for mouse- and rat-sized phantoms were measured for different energy and timing windows. Mouse imaging was optimized with a wide open energy window (150–750 keV) and a 10 ns timing window, leading to a sensitivity of 3.3% at the centre of the FOV and a peak NEC rate of 235 000 cps for a total activity of 80 MBq (2.2 mCi) in the phantom. Rat imaging, due to the higher scatter fraction, and the activity that lies outside of the field of view, achieved a maximum NEC rate of 24 600 cps for a total activity of 80 MBq (2.2 mCi) in the phantom, with an energy window of 250–750 keV and a 6 ns timing window. The sensitivity at the centre of the FOV for these settings is 2.1%. This work demonstrates that different scanner settings are necessary to optimize the NEC count rate for different-sized animals and different injected doses. Finally, phantom and *in vivo* animal studies are presented to demonstrate the capabilities of microPET II for small-animal imaging studies.

1. Introduction

Dedicated small-animal PET systems have been developed by a number of groups and companies (for example, Bloomfield *et al* (1997), Cherry *et al* (1997), Del Guerra *et al* (1998), Jeavons *et al* (1999), Knoess *et al* (2003), Lecomte *et al* (1996), Seidel *et al* (2002), Tai *et al* (2001), Watanabe *et al* (1997), Weber *et al* (1997), Ziegler *et al* (2001)) and have been successfully used in biomedical research over the past ten years. Applications of interest have included drug and tracer development, longitudinal studies of animal models of human disease, and imaging of gene expression, gene therapy, protein function and cell trafficking (Budinger *et al* 1999, Cherry and Gambhir 2001, Phelps 2000).

The initial success and considerable potential of small-animal PET as a tool in modern biomedical research has been the driving force to developing systems with much higher spatial resolution (Correia *et al* 1999, Chatziioannou *et al* 2001, Miyaoka *et al* 2001) and sensitivity (Huber and Moses 1999). In this paper we report on microPET II, a second-generation microPET scanner, with more than a factor of 4 better spatial resolution and higher sensitivity compared with the original microPET system developed in our laboratory in 1996 (Cherry *et al* 1997, Chatziioannou *et al* 1999). The design and development of the microPET II scanner, including a limited set of performance data, has been published previously (Tai *et al* 2003). We now present detailed performance data, including a comparison of different reconstruction algorithms and their effect on image resolution, and the optimization of scanner settings (timing window and energy window) for best noise-equivalent count (NEC) rate performance. Based on these characterization and optimization studies, we also present phantom and *in vivo* animal studies that demonstrate the capabilities of this new small-animal PET scanner.

2. MicroPET II: system description

The microPET II scanner has been described in detail in a previous paper (Tai *et al* 2003), therefore only a brief summary relevant to the measurements reported in this paper will be provided here. The microPET II detectors consist of an array of 14 $\times$ 14 lutetium oxyorthosilicate (LSO) crystals, each measuring 0.975 mm $\times$ 0.975 mm in cross section by 12.5 mm in length. The crystal pitch is 1.15 mm in both the axial and transaxial directions. A Hamamatsu H7546 64-channel photomultiplier tube (PMT) is used as the photon detector (Yoshizawa *et al* 1997, Shao *et al* 2000) and was coupled to the LSO arrays using a fibre-optic bundle (Chatziioannou *et al* 2001, Cherry *et al* 1996) to avoid gaps due to the inactive perimeter of the PMT. The 64 anode signals from each PMT were converted into four position-encoded signals by a resistive readout network and a summing board (Siegel *et al* 1996) and sent to the data acquisition electronics developed for the Concorde microPET® scanner (Tai *et al* 2001). The scanner consists of 90 detector modules arranged in 3 rings, with 30 detector modules in each ring. This leads to a total of 17 640 LSO crystals arranged in 42 rings with 420 crystals in each ring. The axial field of view (FOV) is 4.9 cm and the transaxial FOV is 8.5 cm. The aperture of the scanner is 15.3 cm in diameter. Figure 1 shows a photograph of the completed microPET II system. The gantry housing the detector modules measures 62 cm $\times$ 62 cm $\times$ 16 cm. The entire gantry was mounted on the top of a Concorde microPET® system base cabinet that contains the processing electronics and power supplies. An animal bed has been attached to the scanner. The axial position of the bed is controlled by the host computer, and the vertical position of the bed is adjusted manually. The data acquisition firmware and software, and data sorting software, were modified from that used by the commercial Concorde microPET® systems. All experiments in this paper are acquired in list mode as 3D (three-dimensional) datasets and are histogrammed into a set of 3D sinograms with a span of 3

Figure 1. Photograph of the microPET II system.

and a ring difference of 41. Normalization is achieved by acquiring a high-statistics scan of a uniformly filled cylinder that fills the field of view. Random events were subtracted from prompt events using the delayed window technique. At present, no corrections are made for attenuation or for scattered radiation.

3. Performance measurements: methods

Basic performance data, including the energy, timing and intrinsic spatial resolution of the microPET II detectors, the dependence of spatial resolution on radial offset for 2D (two-dimensional) filtered backprojection reconstruction, and measurements of system sensitivity for default energy and timing windows, can be found in the publication by Tai *et al* (2003). Here, we characterize the spatial resolution for three different reconstruction methods, and measure the sensitivity and noise-equivalent count (NEC) rate for a range of energy and timing windows to determine optimal settings for imaging mice (weight range ∼20–30 g) and rats (weight range ∼200–500 g).

3.1. Spatial resolution

We compared the performance of the following three algorithms for reconstructing data from microPET II.

- *FBP*. Fourier rebinning (FORE) followed by 2D filtered backprojection (FBP): the 3D sinograms were Fourier rebinned (Defrise *et al* 1997) and reconstructed by conventional 2D filtered backprojection with a ramp filter cutoff at the Nyquist frequency. An image matrix size of 256 × 256 pixels was used with a pixel size of 0.2 mm. Eighty-three

contiguous 2D image slices were produced with a centre-to-centre slice spacing of 0.58 mm.

- *OSEM*. The 3D sinogram dataset was rebinned by FORE into a 2D sinogram set and reconstructed with an ordered subsets expectation maximization (OSEM) algorithm. Images were reconstructed on a 256 × 256 matrix with an image pixel size of 0.2 mm. Four iterations and 16 subsets were used. Eighty-three contiguous 2D image slices were produced with a centre-to-centre slice spacing of 0.58 mm.
- *MAP*. The 3D sinogram dataset was reconstructed using a fully 3D *maximum a posteriori* (MAP) algorithm containing an accurate system model. Images were reconstructed into voxels with dimensions 0.2 × 0.2 × 0.58 mm^3 on a 256 × 256 × 83 image matrix. Reconstructions were terminated after 30 iterations.

The FBP and OSEM reconstructions are the standard algorithms provided with the commercial Concorde microPET® scanners. For OSEM, the number of subsets and iterations were determined empirically (data not shown) based on the parameters that were qualitatively observed to lead to good image quality for object sizes and count densities typical in microPET II animal studies. The MAP code is a modification of the algorithm originally developed and validated for the first microPET scanner (Qi *et al* 1998, Chatziioannou *et al* 2000). One feature of microPET II is that there are relatively large gaps between detector blocks, comparable to the size of a crystal. The detector gaps introduce discontinuities in the sinogram (Tai *et al* 2003). This implementation of MAP specifically accounts for the variable detector spacing and the polygonal, rather than circular, geometry of the detector ring. The position-dependent detector response is modelled in a geometric projection matrix by computing the solid angle spanned from each image voxel to the surface of the detector pairs. The photon non-colinearity, inter-crystal penetration and inter-crystal scatter are modelled as a 2D space-variant blurring operation in sinogram space (Qi *et al* 1998). MAP images are computed using a preconditioned conjugate gradient method applied to a posterior density that includes a shifted-Poisson model for randoms corrected coincidence data (Yavuz and Fessler 1998) and a quadratic prior energy function with a spatially varying weighting designed to achieve approximately uniform reconstructed image resolution (Qi and Leahy 2000). Two different values of this weighting ($\beta = 0.1$ and $\beta = 0.01$) were compared (a value of $\beta = 0$ corresponds to standard maximum likelihood reconstruction). Reconstruction was terminated after 30 iterations. It was determined that there was no significant improvement in image resolution after 30 iterations (data not shown).

Both the MAP and OSEM methods that we have implemented use a positivity constraint that prevents the images taking on negative values. This has the effect of artificially improving resolution when reconstructing a point or line source in air. Consequently, a fair comparison of resolution between positively constrained iterative methods and methods based on filtered backprojection, requires that we image a line or point source in a warm background. A resolution phantom was constructed specifically for these measurements. The phantom consisted of two line sources, containing a high radioactivity concentration, placed inside a cylinder with a uniform low-activity background. The cylinder was 2.5 cm in diameter and 4 cm in length. The two line sources were made from steel needles with an inner diameter of 100 μm and an outer diameter of 200 μm. One needle was at the centre of the cylinder, the other offset by 1 cm radially. The needles and the cylinder were filled with $^{18}F^-$ solution at a concentration of about 1800 MBq ml^{-1} and 1.8 MBq ml^{-1} respectively, leading to an intensity ratio in the reconstructed images ranging from 3:1 to 10:1. For the radial and tangential resolution measurements, data were acquired with the cylinder at three different radial locations, 0, 5 and 10 mm from the centre of the scanner, with the needles parallel to

the central axis. This provides image resolution measurements at radial offsets of 0, 5, 10, 15 and 20 mm. Between 260 and 520 $\times$ 10^6 counts were acquired in 60 min for each phantom measurement.

Radial and tangential profiles were drawn through the centre of the image of the reconstructed line sources, the background was subtracted, and the full width at half maximum (FWHM) of the profiles was obtained through linear interpolation. The FWHM of 20 consecutive central planes (planes 31 to 50) was averaged to calculate the image resolution.

For measurement of the axial resolution, the phantom was placed in the scanner with the line sources perpendicular to the central axis of the scanner and with the central line source aligned with the central transaxial image plane. For all three reconstruction algorithms, the transaxial slices were defined to have a thickness of one half the detector pitch, or 0.58 mm, to enable a fair comparison between them. The 2D FBP and OSEM algorithms cannot be 'zoomed' in the axial direction, by definition slices are defined by the detector pitch. This leads to undersampling of the axial profiles used to determine resolution. To compensate for this undersampling, phantom data were acquired in three positions, with the phantom translated along the axial direction by a step size of 0.2 mm between scans (Tai *et al* 2001). Axial profiles of the central needle source from the three measurements were interleaved to obtain axial profiles sampled at 0.2 mm intervals. The background was subtracted, and the FWHM of the profiles was obtained through linear interpolation. Axial resolution profiles were obtained at several different radial offsets along the length of the needle. Results were averaged across five sagittal planes to reduce measurement variability due to sampling fluctuations. Around 300 $\times$ 10^6 counts were acquired for each measurement.

3.2. Sensitivity

A point source was made by enclosing a drop of $^{18}F^-$ solution in a glass capillary with an inner diameter of 1 mm and a wall thickness of 0.2 mm. The point source was placed in the centre field of view (CFOV) of the microPET II scanner and data were acquired for 1 min. Measurements were performed for 24 energy windows, using lower energy thresholds of 150, 200, 250, 300, 350, 400 keV and upper energy thresholds of 650, 700, 750, 800 keV at a fixed coincidence timing window of 10 ns. Measurements were repeated for five different coincidence timing windows (4, 6, 10, 14 and 18 ns) at a fixed energy window of 250 to 750 keV. The activity in the point source ranged from 80 μCi to 25 μCi during the measurements and was measured in a calibrated well counter. The collected data were sorted with a maximum ring difference of 41. The prompt and random coincidence counts were measured simultaneously and the true coincidence counts obtained by subtracting random counts from the prompt counts. The sensitivity was defined as the ratio of the recorded true coincidence counts to the number of positron-emitting decays from the source during the acquisition time. The background coincidence counts due to natural ^{176}Lu decay within the LSO were subtracted, and the branching ratio of $^{18}F^-$ (96.73%) and system dead time (<5%) were accounted for in the calculation of the point source sensitivity.

3.3. Scatter fraction

MicroPET II is designed solely for imaging small laboratory animals of which the most common species by far are mice and rats. Therefore, we estimated the scatter fraction for phantoms that approximate a mouse and rat in size and shape. Both phantoms were made of a solid right cylinder of plexiglass. The mouse-sized phantom was 7 cm long and 2.5 cm in diameter. A hole of 2 mm diameter was drilled parallel to the central axis at a radial distance of 1 cm. The rat-sized phantom was 15 cm long and 6 cm in diameter. A hole of 2 mm

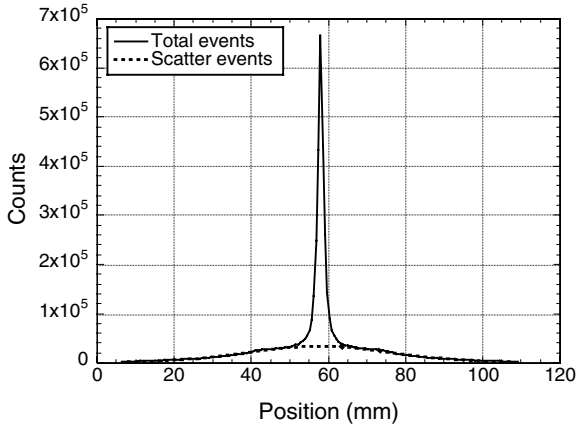

Figure 2. Aligned and summed projection of sinograms from an off-centre line source in a scattering medium. The scatter events are estimated by fitting the projection tails up to +/−1 cm from the centre with a Gaussian function.

diameter was drilled at a radial distance of 2 cm. Capillary tubes of 1 mm inner diameter and 0.2 mm wall thickness, filled with $^{18}F^{-}$ solution, were inserted into the holes. The phantoms were placed at the centre of the scanner. For each phantom, measurements were performed for lower energy thresholds of 150, 250, 350 and 450 keV, with a fixed upper energy threshold of 750 keV. The measured data were sorted by single-slice rebinning, with a maximum ring difference of 41, and randoms were subtracted. All projection elements in the sinogram located farther than 1.75 cm from the centre for the mouse-sized phantom, and 3.5 cm from the centre for the rat-sized phantom, were set to zero. For each projection angle within the sinogram, the location of the centre of the line source was determined by finding the projection element containing the largest number of counts. Each projection angle was then shifted so that the projection element containing the maximum value was aligned with the central column of the sinogram. After alignment, the projection angles of all slices (planes) were summed to create a single profile. The scattered counts under the peak were then determined by fitting the tail of the profile, up to +/−1 cm from the centre of the profile in both sides with a Gaussian function as shown in figure 2. The scatter fraction is the ratio of the scattered counts to the total counts.

3.4. Count-rate performance

Hollow cylindrical phantoms with the same outer dimensions as the cylinders used for the scatter fraction measurements were used to measure count-rate performance. The phantoms were filled with $^{18}F^{-}$ solution with initial activity of 207 MBq (5.6 mCi) for the mouse-sized phantom (total volume 34 cc) and 455 MBq (12.3 mCi) for the rat-sized phantom (total volume 424 cc), and scanned over ten half-lives with nine different combinations of energy and timing windows. The lower energy threshold ranged from 150–350 keV and the timing window from 6–14 ns. The upper energy threshold was fixed at 750 keV for these measurements. The parameter ranges were chosen based on the results of the sensitivity measurements obtained in section 3.2. The true (T), scatter (S) and noise-equivalent (NEC) counting rates were calculated from the measured prompt (P) and random (R) counting rates by the following equations,

$$T = (P - R) \times (1 - \mathrm{SF}) \tag{1}$$

$$S = (P - R) \times \mathrm{SF} \tag{2}$$

$$\mathrm{NEC} = \frac{T^2}{T + S + 2kR} \tag{3}$$

where SF is the scatter fraction measured in the previous section and k is the fraction of the transverse FOV occupied by the phantom (Strother *et al* 1990). For the mouse-sized and rat-sized phantoms, k is 0.294 and 0.706 respectively.

4. Imaging studies: methods

For all studies described below, 3D list mode data were acquired and reconstructed with either FORE followed by 2D FBP (ramp filter, cutoff at Nyquist frequency), or with 3D MAP with a β value ranging from 0 to 0.4 and 30 iterations. β values of 0.01 to 0.1 typically are used to reconstruct high count, high contrast studies, and β values of 0.1 to 0.4 are commonly employed for lower contrast and/or lower count density datasets. Normalization was based on a high-statistics scan of a uniformly filled cylinder. No attenuation or scatter correction was applied. All animal studies were carried out under anaesthesia (1–2% isoflurane) using protocols approved by the UC Davis animal care committee. According to the NEC optimizations carried out in section 3.4, an energy window of 150 to 750 keV and a timing window of 10 ns were used for all mouse studies, and an energy window of 250 to 750 keV and a timing window of 10 ns were used for all rat studies.

4.1. Derenzo phantoms

A miniature Derenzo hot-rod phantom was scanned on both the microPET II and Concorde microPET® P4 (Tai *et al* 2001) systems. Rod diameters in the six sections are 0.8, 1.0, 1.25, 1.5, 2.0 and 2.5 mm, respectively, and the centre-to-centre separations are twice the rod diameter. The phantom was filled with 22 MBq (0.6 mCi) of $^{18}F^-$ and scanned for 60 min in the microPET II system, followed by a scan of duration 100 min in the Concorde microPET® P4 system to keep the number of decays about the same in the two scans. Approximately 700 million events were acquired on both scanners.

A miniature Derenzo cold-rod phantom was also scanned on both systems. Rod diameters in the six sections are 1.2, 1.6, 2.4, 3.2, 4.0 and 4.8 mm, respectively, and centre-to-centre separations are twice the rod diameter. The phantom was filled with 37 MBq (1 mCi) $^{18}F^-$ and scanned for 60 min in the microPET II system followed by 100 min in the Concorde microPET® P4 system. Approximately 800 million events were acquired on both scanners.

4.2. Bone metabolism: mouse and rat whole-body imaging

A 31 g mouse was injected with 37 MBq (1 mCi) of $^{18}F^-$ and scanned over two bed positions. The scan was started 180 min after injection and lasted 60 min for each bed position. In total 311 million counts were acquired for the two bed positions. Images were reconstructed using MAP with β equal to 0 (corresponding to maximum-likelihood reconstruction, MLEM).

A 304 g rat was injected with 107 MBq (2.9 mCi) of $^{18}F^-$ and scanned over five bed positions. The scan was started 210 min after injection and lasted 20 min for each bed position. In total 202 million counts were acquired for the five bed positions. Images were reconstructed using MAP with β equal to 0 (MLEM).

4.3. Glucose utilization: mouse and rat brain

A 32 g mouse was injected with 21 MBq (0.58 mCi) of ^{18}FDG. The mouse brain was scanned for 60 min, starting 40 min after injection. A total of 163 million counts were acquired. Images were reconstructed by MAP with β equal to 0.4.

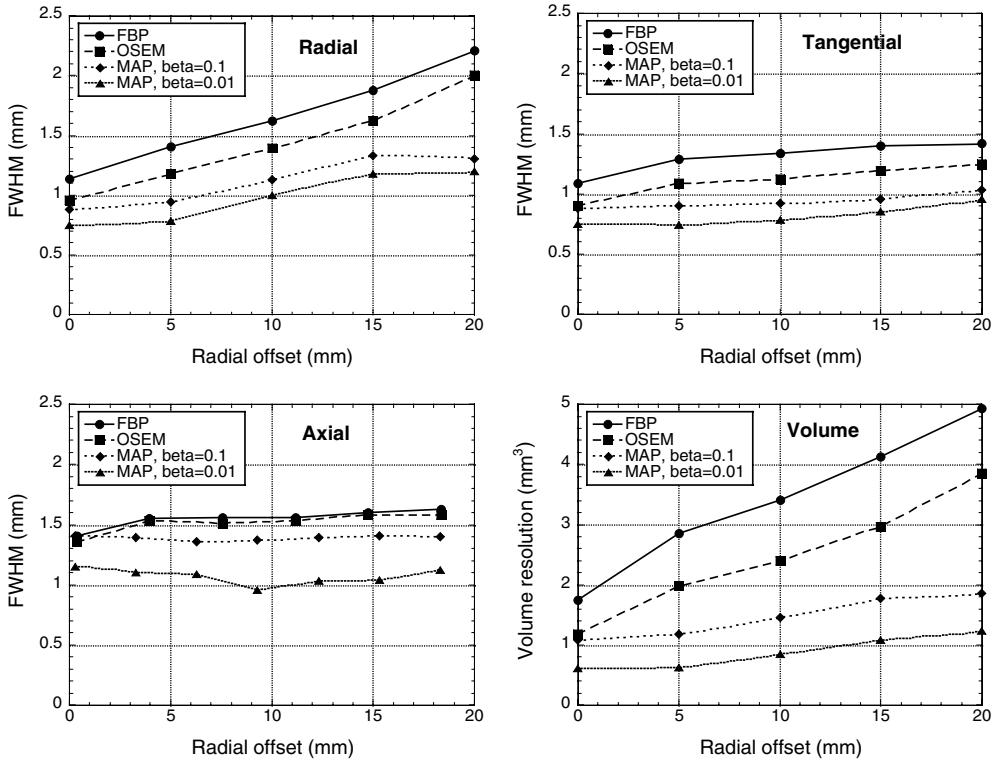

Figure 3. Image resolution of microPET II using FBP, OSEM and MAP reconstructions.

A 309 g rat was injected with 31 MBq (0.84 mCi) of ^{18}FDG. The rat brain was scanned for 60 min, starting 60 min after injection. A total of 97 million counts were acquired. Images were reconstructed by MAP with β equal to 0.4.

4.4. Glucose utilization: mouse and rat heart

A 32 g mouse was injected with 21 MBq (0.58 mCi) of ^{18}FDG. The mouse heart was scanned for 60 min, starting 120 min after injection. A total of 219 million counts were acquired. Images were reconstructed by MAP with β equal to 0.1.

A 300 g rat was injected with 81 MBq (2.2 mCi) of ^{18}FDG. The rat heart was scanned for 60 min, starting 40 min after injection. A total of 433 million counts were acquired. Images were reconstructed by MAP with β equal to 0.1.

5. Performance measurements: results

5.1. Image resolution

Figure 3 shows radial, tangential, axial and volumetric resolutions at different radial offsets for FBP, OSEM and MAP reconstructions. The volumetric resolution is defined as the product of radial, tangential and axial resolutions. As expected, the radial resolution increases with increasing radial offset due to depth of interaction effects, whereas the tangential resolution is

Table 1. CFOV sensitivity (%) of microPET II for different energy windows. The timing window is 10 ns.

	Upper energy threshold (keV)			
Lower energy threshold (keV)	650	700	750	800
150	3.23	3.29	3.28	3.30
200	2.66	2.73	2.74	2.73
250	2.21	2.28	2.29	2.29
300	1.78	1.81	1.84	1.86
350	1.39	1.45	1.46	1.49
400	1.09	1.14	1.16	1.17

much less dependent on radial offset. The axial resolution is generally the worst of the three components. This is thought to be due to depth of interaction effects in the axial direction that occur in 3D datasets with large acceptance angles. This effect will be worst in the centre of the axial field of view, which is where the axial resolution was measured. The volumetric resolution averaged across a 3 cm diameter transverse field of view (roughly the size of a mouse) is 3.2 μl (FBP), 2.2 μl (OSEM), 1.4 μl (MAP, $\beta = 0.1$) and 0.8 μl (MAP, $\beta = 0.01$). The iterative algorithms provide higher spatial resolution than filtered backprojection. The differences between OSEM and MAP results are likely a consequence of the detailed system model utilized in the MAP algorithm, which accurately models the geometry of the scanner. The results obtained from the resolution phantom (line source in warm background) are slightly worse (2.8 μl versus 2.1 μl at a radial position of 5 mm) than that measured with a line source in air (Tai *et al* 2003) for filtered backprojection reconstruction. This small degradation is probably caused by scatter in the resolution phantom. The radial resolution of MAP at a radial offset of 20 mm is better than the general trend of the curves predicts is likely. It was found that the edge of the resolution phantom in the images reconstructed by MAP is slightly deformed, because the edge of the phantom is very close to the edge of the 256 $\times$ 256 image matrix. This probably affected the measured radial resolution. A similar effect was also observed for OSEM reconstructions. The radial resolution of OSEM at radial offset of 20 mm was therefore obtained using a 512 $\times$ 512 image matrix with the same (0.2 mm) pixel size so that the line source is not located at the edge of the image for the 20 mm offset case. It is not practical to do the same for MAP, as the computational requirements become unreasonable for such a large matrix size.

5.2. Sensitivity

Table 1 shows the absolute sensitivity at the CFOV for different energy windows with a timing window of 10 ns. The sensitivity is a strong function of the lower energy threshold in the 150–300 keV range, but as expected, a very weak function of the upper energy threshold above 650 keV. MicroPET II has an absolute sensitivity of about 2.3% and 3.3% for lower energy thresholds of 250 and 150 keV respectively. Table 2 shows absolute sensitivity for different timing windows at an energy window of 250–750 keV. The sensitivity increases by a factor of 2 as the timing window is changed from 2 to 6 ns, but only increases a further 10% when the timing window is increased to 10 ns. There is little gain in sensitivity by increasing the timing window beyond 10 ns. These results are consistent with the measured detector timing resolution of 3.0 ns (Tai *et al* 2003).

Table 2. CFOV sensitivity of microPET II for different coincidence timing windows. The energy window is 250 to 750 keV.

Timing window (ns)	Sensitivity (%)
2	0.96
6	2.07
10	2.29
14	2.31
18	2.31

Table 3. Scatter fraction (SF) for mouse-sized and rat-sized phantoms.

Phantom	Energy window	SF (%)
25 mm $\phi \times$ 70 mm	150–750 keV	12.8
(34 cc)	250–750 keV	9.7
	350–750 keV	7.2
	450–750 keV	5.3
60 mm $\phi \times$ 150 mm	150–750 keV	53.7
(424 cc)	250–750 keV	45.6
	350–750 keV	35.9
	450–750 keV	23.3

5.3. Scatter fraction

Table 3 shows the scatter fraction as a function of lower energy threshold for the mouse-sized phantom and the rat-sized phantom. As expected, the scatter fraction increases as the phantom volume increases and as the lower energy threshold decreases. These scatter fractions are consistent with those measured previously for small-animal systems and show that for a rat-sized object, the scatter fraction can be very significant (20–50%). These measured scatter fraction values are used to calculate the NEC rates presented in the next section.

5.4. Count-rate performance

Figure 4 shows total (prompt) counting rates, random counting rates and the calculated NEC curves from the mouse-sized phantom for different energy and timing windows. The peak total counting rates were around 700 000 cps at which point saturation is clearly seen (discontinuity in the curves). The activity at which saturation occurs depends strongly on the energy and timing window, and occurs as low as 2.4 MBq cc^{-1} (corresponding to 82 MBq of activity in the cylinder) for a 150–750 keV energy window and a 14 ns timing window. The increase in randoms counting rate with activity depends more strongly on the lower energy threshold than the timing window. For the mouse-sized phantom, the best NEC performance across the entire range of typical injected doses is to use an energy window of 150–750 keV and a timing window of 10 ns. For these settings, the NEC curve peaks at 235 000 cps at an activity concentration of around 2.35 MBq cc^{-1} ($\sim$80 MBq in the phantom). This wide-open energy window maximizes sensitivity, and because the scatter fraction for mouse imaging is low, the increase in sensitivity outweighs the increase in scatter. The timing window can also be left wide open (even for a 14 ns window, the NECs are only reduced slightly towards the top of the injected dose range), because there is only a small amount of activity outside the field of view, and therefore the coincidence to singles ratio is quite favourable. Generally, for mouse imaging, NEC rates achieved will be limited by the injected dose that is administered

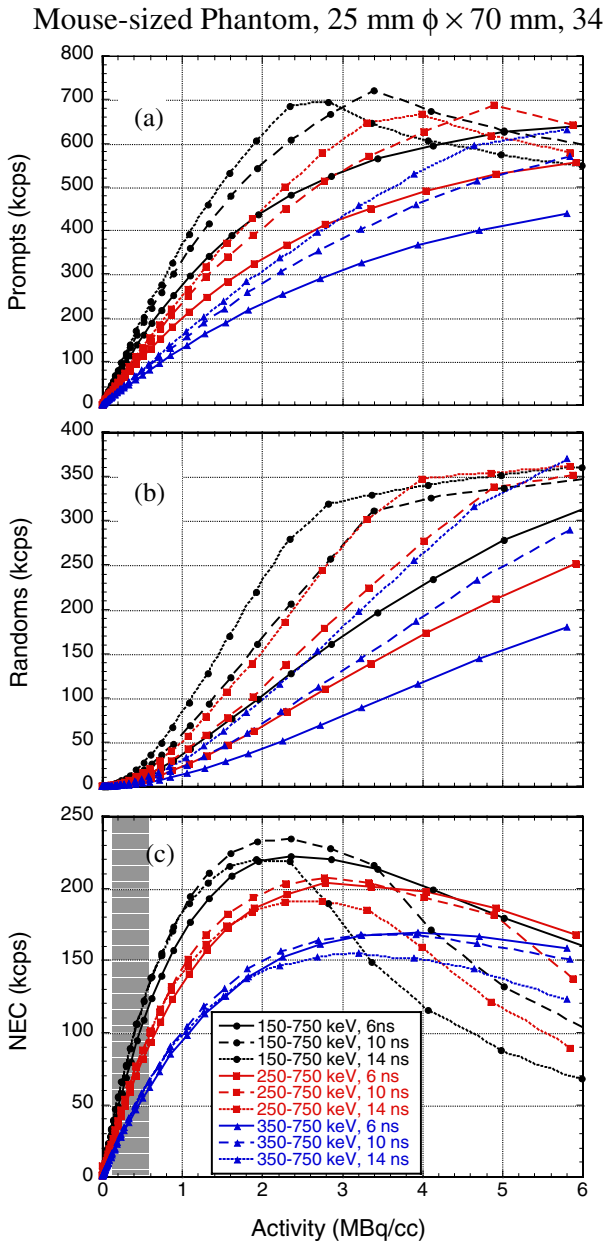

Figure 4. Prompt coincidence (a), random (b) and NEC (c) counting rates of microPET II for a mouse-sized phantom for different energy and timing windows. Shaded area in (c) indicates the typical injected dose range for mouse studies.

(typically in the range 3.7–37 MBq, limited by the volume of the injectate, specific activity of the radiopharmaceutical, and by concerns regarding mass effects) and not by count-rate limitations of the scanner.

Figure 5 shows the total counting rate, random counting rate and NEC curves for the rat-sized phantom. Different trends are observed, primarily due to an increase in random coincidence events and scattered events because much of the phantom extends beyond the

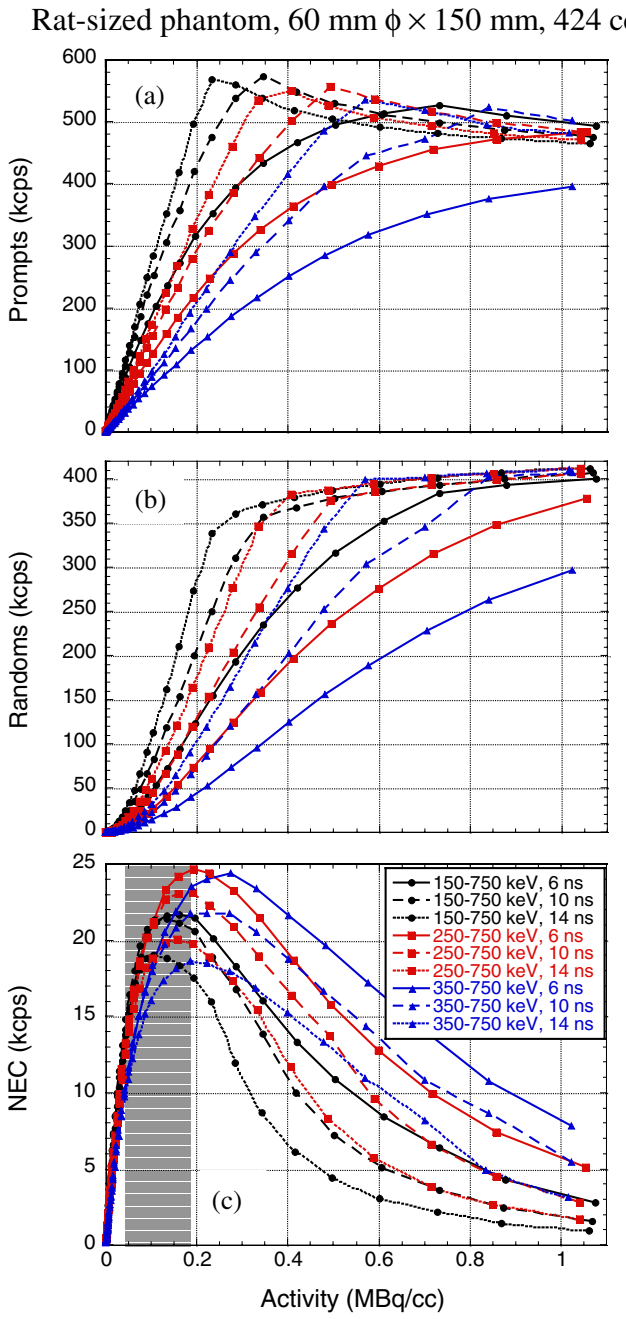

Figure 5. Prompt coincidence (a), random (b) and NEC (c) counting rates of microPET II for a rat-sized phantom for different energy and timing windows. Shaded area in (c) indicates the typical injected dose range for rat studies.

axial FOV of the scanner in a region that is difficult to shield, and because the volume of the phantom is more than a factor of 10 larger. The peak total counting rate is reduced to about 550 kcps due to the larger number of random coincidences. The peak NEC counting rate of 24 600 cps is achieved at an activity concentration of 0.19 MBq cc^{-1} (∼80 MBq in phantom)

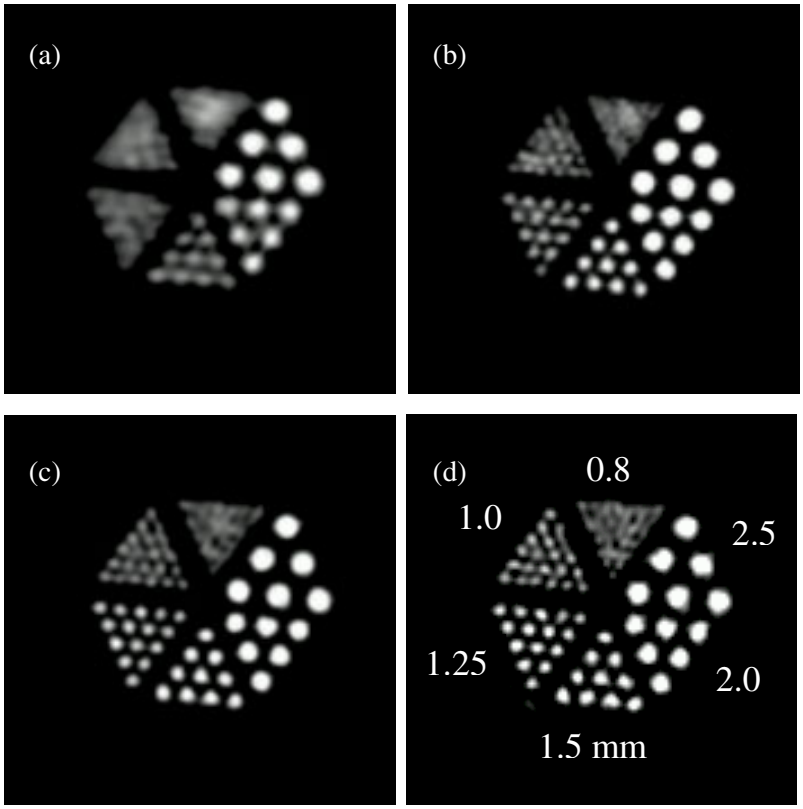

Figure 6. Images of a miniature Derenzo hot-rod phantom. The rod diameters are shown in (d). The centre-to-centre separations are twice the rod diameter. The phantom was filled with 22 MBq (0.6 mCi) $^{18}F^{-}$ and scanned for 60 min. (a) Image measured by Concorde P4 scanner and reconstructed by FBP. (b) Image measured by microPET II and reconstructed by FBP. (c) Image measured by microPET II and reconstructed by MAP with β of 0.1. (d) Image measured by microPET II and reconstructed by MAP with β of 0.01.

with an energy window of 250–750 keV, and a timing window of 6 ns. Notably, the optimal energy and timing windows vary across the range of typical injected doses. For example, at low doses (concentrations <0.1 MBq cc^{-1}, activity 'injected' in phantom <42 MBq), the 150–750 keV energy window and 10 ns timing window provide the best NEC performance. At higher doses (concentrations of between 0.1 and 0.24 MBq cc^{-1}, corresponding to 'injected' activities of between 42 and 100 MBq) a 250–750 keV energy window and 6 ns timing window provide the highest NEC rate. It is also clear that for rat imaging, NEC performance is being impacted by system count-rate limitations for injected doses towards the high end of the range. However, it should be noted that all these studies were conducted with no attempt to shield out of FOV activity.

6. Imaging studies: results

6.1. Derenzo phantoms

Figure 6 shows a transverse slice of the miniature Derenzo hot-rod phantom reconstructed from data taken on the Concorde P4 microPET scanner and on the microPET II scanner for

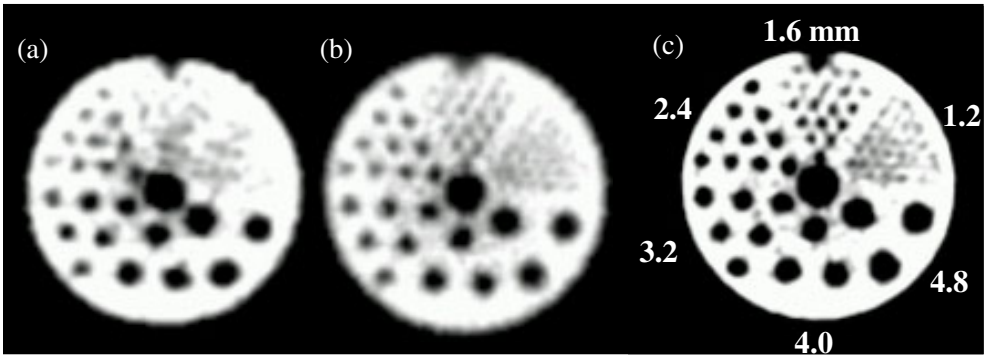

Figure 7. Images of a miniature Derenzo cold-rod phantom. The rod diameters are shown in (c). The centre-to-centre separations are twice the rod diameter. The phantom was filled with 37 MBq (1 mCi) $^{18}F^{-}$, and scanned for 60 min. (a) Image measured by Concorde P4 and reconstructed by FBP. (b) Image measured by microPET II and reconstructed by FBP. (c) Image measured by microPET II and reconstructed by MAP with β of 0.4.

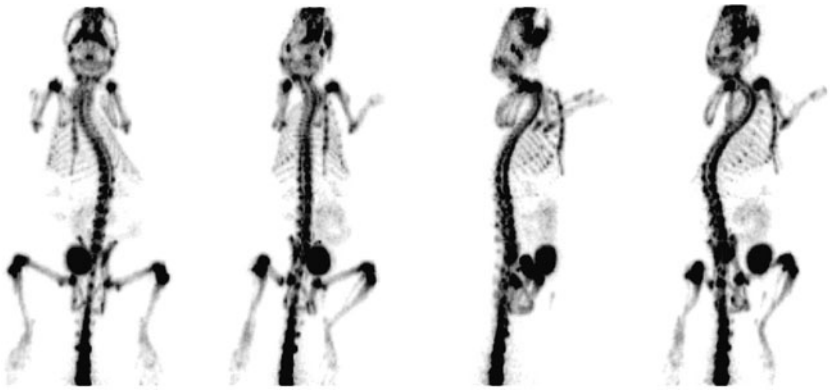

Figure 8. Projection views of bone scan of a 31 g mouse injected with 37 MBq (1 mCi) of $^{18}F^{-}$, scanned across two bed positions at 60 min per bed position, starting 180 min after injection. Image reconstructed by MAP with β equal to 0 (MLEM).

different reconstruction algorithms. Using FBP reconstruction, the Concorde P4 microPET® system can resolve the 1.5 mm diameter rods, and the microPET II system can resolve rods that are 1.25 mm in diameter. Using MAP reconstruction, rods as small as 1 mm diameter can be easily resolved with the microPET II system. Figure 7 shows a transverse slice through the miniature Derenzo cold-rod phantom. The cold-rod phantom is a much more difficult object to image as it provides an evaluation of both resolution and contrast. With the Concorde P4 microPET, the smallest rods that are clearly resolved with FBP reconstruction are the 2.4 mm rods. With microPET II, rods as small as 1.6 mm can be resolved, and with MAP reconstruction ($\beta = 0.4$, corresponding to a volumetric resolution of 1.5 μl at CFOV), it is possible to resolve some of the 1.2 mm rods.

6.2. Bone metabolism: mouse and rat whole-body imaging

Figures 8 and 9 show maximum intensity projection views of $^{18}F^{-}$ bone images of a mouse and a rat respectively. The individual ribs of the mouse and rat can be clearly identified, even

Figure 9. Maximum intensity projection views of bone scan of a 304 g rat injected with 107 MBq (2.9 mCi) of $^{18}F^{-}$, scanned across five bed positions at 20 min per bed position, starting 210 min after injection. Image reconstructed by MAP with β equal to 0 (MLEM).

though no cardiac or respiratory gating was employed. Increased $^{18}F^{-}$ uptake is apparent in the growth plates of the bones (especially visible in the wrist and joints in the limbs) indicating, unlike humans, that there is continued growth of the bones in rodents into adulthood. These studies show the potential of microPET II for imaging high contrast objects, where the full resolving power of the instrument can clearly be appreciated.

6.3. Glucose utilization: mouse and rat brain

Figures 10 and 11 show coronal sections through FDG images of the mouse and rat brain. Images are reconstructed with a β value of 0.4 which corresponds to a volumetric resolution of approximately 1.5 μl at CFOV. In the rat, enhanced uptake is evident in the cortex, thalamus and striatum. There also is uptake in many extracerebral areas, including muscle, harderian glands and salivary glands. In the mouse, due to the small width of the white matter tracts, visualization of major brain structures is still limited, even though the brain covers many resolution elements (mouse brain is approximately 450 mm^3 $\approx$ 450 resolution elements). However, the resolution should be sufficient for quantifying activity in major brain structures, assuming the structures can be located through the use of a stereotactic head-holder and/or registration to a mouse brain atlas.

6.4. Glucose utilization: mouse and rat heart

Figures 12 and 13 show transverse, coronal and sagittal views of FDG heart images of a mouse and a rat. No cardiac gating was applied in these studies. The two heart chambers can be clearly identified with particularly clear demarcation of the left ventricular wall, even in the mouse where the diameter of the left ventricle is only around 6 mm. Once again, in this high contrast scenario, the resolution of the scanner can be clearly appreciated.

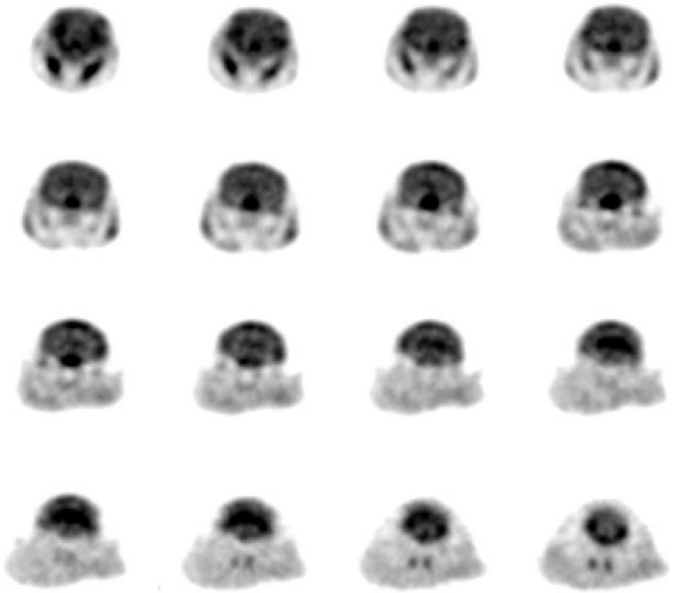

Figure 10. Transverse slices from brain image of a 32 g mouse injected with 21 MBq (0.58 mCi) of ^{18}FDG, scanned for 60 min, starting 40 min after injection. Image reconstructed by MAP with β equal to 0.4.

Figure 11. Transverse slices from brain of a 309 g rat injected with 31 MBq (0.84 mCi) of ^{18}FDG, scanned for 60 min, starting 60 min after injection. Image reconstructed by MAP with β equal to 0.4.

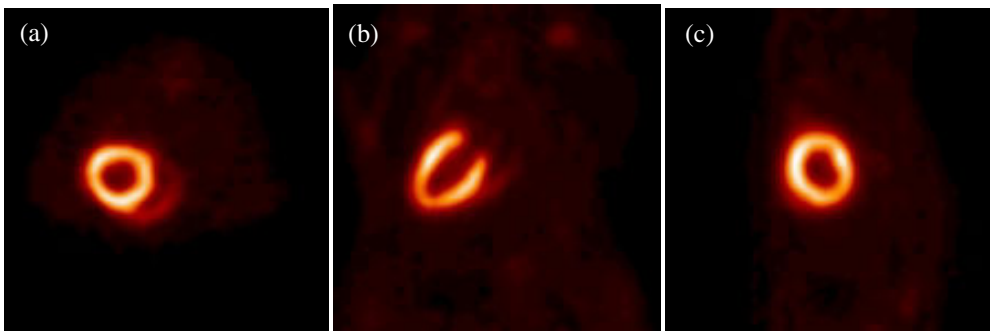

Figure 12. Transverse (a), coronal (b) and sagittal (c) views of heart images of a 32 g mouse injected with 21 MBq (0.58 mCi) of ^{18}FDG, scanned for 60 min, starting 120 min after injection. Image reconstructed by MAP with β equal to 0.1.

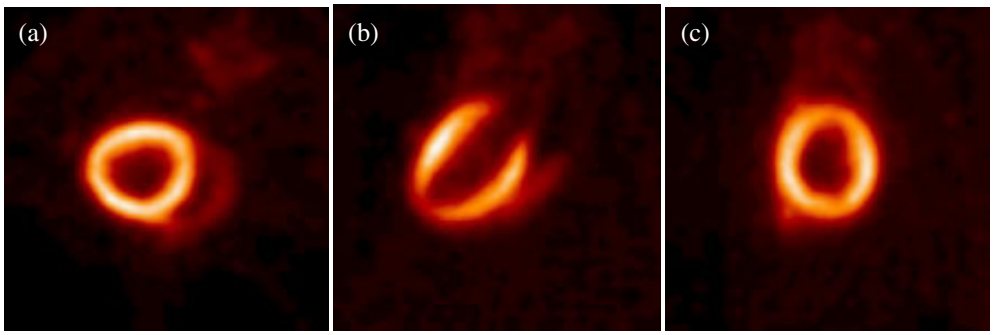

Figure 13. Transverse (a), coronal (b) and sagittal (c) views of heart images of a 300 g rat injected with 81 MBq (2.2 mCi) of ^{18}FDG, scanned for 60 min, starting 40 min after injection. Image reconstructed by MAP with β equal to 0.1.

7. Discussion and conclusion

The microPET II system has now been used in a range of animal studies and has proved very stable over the past year of continuous operation. Our performance evaluation indicates that microPET II meets its design specifications of 1 μl reconstructed resolution for a mouse-sized object when used in conjunction with a MAP reconstruction algorithm that accurately models system geometry and other physical processes that impact the localization of the annihilation photons. The sensitivity is a strong function of the lower energy threshold in the 150–300 keV range, but a very weak function of the upper energy threshold above 650 keV. A timing window of 10 ns is sufficient to include virtually all true coincidence events. The sensitivities at the CFOV are 2.3% and 3.3% for energy windows of 250 to 750 keV and 150 to 750 keV respectively, when the timing window is 10 ns. These represent very significant improvements in both sensitivity and resolution (roughly a factor of 4 in both cases) compared with our first microPET prototype (Cherry *et al* 1997, Chatziioannou *et al* 1999).

The counting-rate performance measurements show that different energy and timing windows should be used to optimize mouse and rat imaging. The peak NEC counts are 235 000 cps and 24 600 cps for a mouse-sized and a rat-sized object, respectively. It should also be noted that the NEC measurements were made with phantoms containing homogeneous activity distributions, which rarely occurs for real animal studies. Furthermore, the NEC

curves are sensitive to the value of the scatter fraction used in equation (3), and the precise methodology for measuring the scatter fraction is open to some debate. Therefore, the NEC data, while useful for guiding optimal settings for timing and energy windows, should not be overinterpreted. Finally, there was no attempt to shield activity outside of the axial field of view and it is likely that incorporating some shielding into the bed design may assist NEC rates, especially in rat studies.

Phantom and animal studies demonstrate the capability of microPET II for small-animal imaging, especially for studies where high spatial resolution is required to resolve small organs or sub-structures within an animal. Future works include further optimization of the MAP reconstruction, development of a component based normalization approach (Bai *et al* 2002, Casey *et al* 1995) and evaluation of quantitative accuracy for *in vivo* studies.

Acknowledgments

The authors thank Evren Asma for assistance with the MAP reconstruction code, and Dr Guido Zavattini, Dr Arion Chatziioannou, Robert Silverman and Jennifer Stickel for useful discussions and technical help. The authors also thank Steven Rendig and Calliandra Harris for their assistance in performing the animal studies. This work was funded by NIH grants R01 EB000561 and R01 EB000363.

References

Bai B, Li Q, Holdsworth C H, Asma E, Tai Y C, Chatziioannou A and Leahy R M 2002 Model-based normalization for iterative 3D PET image reconstruction *Phys. Med. Biol.* **47** 2773–84

Bloomfield P M, Myers R, Hume S P, Spinks T J, Lammertsma A A and Jones T 1997 Three-dimensional performance of a small-diameter positron emission tomograph *Phys. Med. Biol.* **42** 389–400

Budinger T F, Benaron D A and Koretsky A P 1999 Imaging transgenic animals *Annu. Rev. Biomed. Eng.* **1** 611–48

Casey M E, Gadagkar H and Newport D 1995 A component based method for normalization in volume PET *Proc. the 1995 Int. Meeting on Fully Three-Dimensional Image Reconstruction in Radiology and Nuclear Medicine* pp 67–71

Chatziioannou A F, Cherry S R, Shao Y, Silverman R W, Meadors K, Farquhar T H, Pedarsani M and Phelps M E 1999 Performance evaluation of microPET: a high-resolution lutetium oxyorthosilicate PET scanner for animal imaging *J. Nucl. Med.* **40** 1164–75

Chatziioannou A, Qi J, Moore A, Annala A, Nguyen K, Leahy R and Cherry S R 2000 Comparison of 3-D maximum a posteriori and filtered backprojection algorithms for high-resolution animal imaging with microPET *IEEE Trans. Med. Imaging* **19** 507–12

Chatziioannou A, Tai Y C, Doshi N and Cherry S R 2001 Detector development for microPET II: a 1 μl resolution PET scanner for small animal imaging *Phys. Med. Biol.* **46** 2899–910

Cherry S R and Gambhir S S 2001 Use of positron emission tomography in animal research *Inst. Lab. Anim. Res. J.* **42** 219–32

Cherry S R, Shao Y, Siegel S, Silverman R W, Mumcuoglu E, Meadors K and Phelps M E 1996 Optical fiber readout of scintillator arrays using a multi-channel PMT: a high resolution PET detector for animal imaging *IEEE Trans. Nucl. Sci.* **43** 1932–7

Cherry S R *et al* 1997 MicroPET: a high resolution PET scanner for imaging small animals *IEEE Trans. Nucl. Sci.* **44** 1161–6

Correia J A, Burnham C A, Kaufman D and Fischman A J 1999 Development of a small animal PET imaging device with resolution approaching 1 mm *IEEE Trans. Nucl. Sci.* **46** 631–5

Defrise M, Kinahan P E, Townsend D W, Michel C, Sibomana M and Newport D F 1997 Exact and approximate rebinning algorithms for 3D PET data *IEEE Trans. Med. Imaging* **16** 145–58

Del Guerra A, Di Domenico G, Scandola M and Zavattini G 1998 YAP-PET: first results of a small animal positron emission tomograph based on YAP:Ce finger crystals *IEEE Trans. Nucl. Sci.* **45** 3105–8

Huber J S and Moses W W 1999 Conceptual design of a high-sensitivity small animal PET camera with 4 pi coverage *IEEE Trans. Nucl. Sci.* **46** 498–502

Jeavons A P, Chandler R A and Dettmar C A R 1999 A 3D HIDAC-PET camera with sub-millimetre resolution for imaging small animals *IEEE Trans. Nucl. Sci.* **46** 468–73

Knoess C *et al* 2003 Performance evaluation of the microPET R4 PET scanner for rodents *Eur. J. Nucl. Med. Mol. Imaging* **30** 737–47

Lecomte R, Cadorette J, Rodrigue S, Lapointe D, Rouleau D, Bentourkia M, Yao R and Msaki P 1996 Initial results from Sherbrooke avalanche photodiode positron tomograph *IEEE Trans. Nucl. Sci.* **43** 1952–57

Miyaoka R S, Kohlmyer S G and Lewellen T K 2001 Performance characteristics of micro crystal element (MiCE) detectors *IEEE Trans. Nucl. Sci.* **48** 1403–7

Phelps M E 2000 Inaugural article: positron emission tomography provides molecular imaging of biological processes *Proc. Nat. Acad. Sci. USA* **97** 9226–33

Qi J and Leahy R M 2000 Resolution and noise properties of MAP reconstructions in fully 3D PET *IEEE Trans. Med. Imaging* **19** 493–506

Qi J, Leahy R M, Cherry S R, Chatziioannou A and Farquhar T H 1998 High-resolution 3D Bayesian image reconstruction using the microPET small-animal scanner *Phys. Med. Biol.* **43** 1001–13

Seidel J, Vaquero J J and Green M V 2002 Resolution uniformity and sensitivity of the NIH ATLAS small animal PET scanner: comparison to simulated LSO scanners without depth-of-interaction capability 2001 *IEEE Nuclear Science Symposium Conference Record* vol 3 (Piscataway, NJ: IEEE) pp 1555–8

Shao Y, Silverman R W and Cherry S R 2000 Evaluation of Hamamatsu R5900 series PMTs for readout of high-resolution scintillator arrays *Nucl. Instrum. Methods* A **454** 379–88

Siegel S, Silverman R W, Shao Y and Cherry S R 1996 Simple charge division readouts for imaging scintillator arrays using a multi-channel PMT *IEEE Trans. Nucl. Sci.* **43** 1634–41

Strother S C, Casey M E and Hoffman E J 1990 Measuring PET scanner sensitivity: relating count rates to image signal-to-noise ratios using noise equivalent counts *IEEE Trans. Nucl. Sci.* **37** 783–8

Tai Y C, Chatziioannou A, Siegel S, Young J, Newport D, Goble R N, Nutt R E and Cherry S R 2001 Performance evaluation of the microPET P4: a PET system dedicated to animal imaging *Phys. Med. Biol.* **46** 1845–62

Tai Y C, Chatziioannou A, Yang Y F, Silverman R W, Meadors K, Siegel S, Newport D, Stickel J R and Cherry S R 2003 MicroPET II: design, development, and initial performance of an improved microPET scanner for small-animal imaging *Phys. Med. Biol.* **48** 1519–37

Watanabe M, Okada H, Shimizu K, Omura T, Yoshikawa E, Kosugi T, Mori S and Yamashita T 1997 A high resolution animal PET scanner using compact PS-PMT detectors *IEEE Trans. Nucl. Sci.* **44** 1277–82

Weber S, Terstegge A, Herzog H, Reinartz R, Reinhart P, Rongen F, Muller -Gartner H W and Halling H 1997 The design of an animal PET: flexible geometry for achieving optimal spatial resolution or high sensitivity *IEEE Trans. Med. Imaging* **16** 684–9

Yavuz M and Fessler J A 1998 Statistical image reconstruction methods for randoms-precorrected PET scans *Med. Imaging Anal.* **2** 369-78369-78

Yoshizawa Y, Ohtsu H, Ota N, Watanabe T and Takeuchi J 1997 The development and the study of R5900-00-M64 for scintillating/optical fiber readout 1997 *IEEE Nuclear Science Symposium Conference Record* vol 1 (Piscataway, NJ: IEEE) pp 877–81

Ziegler S I, Pichler B J, Boening G, Rafecas M, Pimpl W, Lorenz E, Schmitz N and Schwaiger M 2001 A prototype high-resolution animal positron tomograph with avalanche photodiode arrays and LSO crystals *Eur. J. Nucl. Med.* **28** 136–43